Journal of Geodesy manuscript No.
(will be inserted by the editor)

Estimating Three-Dimensional Displacements with InSAR: the Strapdown Approach

Wietske Brouwer · Ramon Hanssen

Version: September 8, 2023

Abstract Deformation phenomena on Earth are inherently three dimensional. With InSAR, in many practical situations the maximum number of observations is two (ascending and descending), resulting in an infinite number of possible displacement estimates. Here we propose a practical solution to this underdeterminancy problem in the form of the strapdown approach. With the strapdown approach it is possible to obtain 3D-global/2D-local solutions, using minimal and largely undisputed contextual information. It is a generic method that defines a local reference system with transversal, longitudinal, and normal (TLN) axes, with displacement occurring in the transversal-normal plane only. Since the orientation of the local frame is based on the physics of the problem at hand, the strapdown approach gives physically more relevant estimates compared to conventional approaches. Moreover, with uncertainty in the orientation of the local frame and error propagation it is possible to assess the precision of the final estimates. Appropriate cartographic visualization using vector map with confidence ellipses enables an improved interpretation of the results.

InSAR, geodesy, surface displacements, decomposition, strapdown

W. S. Brouwer
Delft University of Technology
Stevinweg 1
2628 CN Delft
E-mail: w.s.brouwer@tudelft.nl

R.F. Hanssen
Delft University of Technology
E-mail: r.f.hanssen@tudelft.nl

1 Introduction

InSAR scatterers are typically not situated at ideal locations, and the observations have an imaging geometry that is not optimal for retrieving full three-dimensional (3D) displacements. Moreover, they are only sensitive to the projection of the 3D displacement vector onto the radar line-of-sight (LoS) direction, d_{LoS}, along a plane orthogonal to the LoS (Massonnet and Feigl, 1998; Fialko et al., 2002; Hanssen, 2001; Wright et al., 2004; Brouwer and Hanssen, 2023b), i.e.,

$$\begin{aligned} d_{\mathrm{LoS}} &= P_{\mathrm{LoS}^{\perp}}\, d_{\mathrm{ENU}}, \\ &= [\sin\theta \sin\alpha_d, \sin\theta \cos\alpha_d, \cos\theta]\, d_{\mathrm{ENU}}, \end{aligned} \tag{1}$$

where $d_{\mathrm{ENU}} = [d_e, d_n, d_u]^T$ is the 3D displacement vector in east, north, and up direction, respectively.[1] $P_{\mathrm{LoS}^{\perp}}$ is the orthogonal projec-

[1] Note that a displacement vector d, in [mm], may also be interpreted as, e.g., an (average or instanta-

tor onto the LoS, where θ is the incidence angle towards the radar, and α_d is the azimuth of its zero-Doppler plane (ZDP) at the position of the target, in the direction towards the satellite, see Brouwer and Hanssen (2023b, Fig. 1).

Ideally, a decomposition of the LoS displacement vector in three orthogonal directions is enabled. Yet, this requires at least three independent LoS observations from significantly different viewing geometries, but since all current SAR satellites have very similar viewing geometries, the maximum number of available and effective observations often reduces to two, i.e., ascending and descending, resulting in an underdetermined problem with an infinite number of solutions along a solution line (Brouwer and Hanssen, 2023b).

Many contemporary InSAR information products, including most publicly available ones, 'circumvent' this problem by disregarding the north component of the deformation, and asserting a decomposition into the east and up components only (Crosetto et al., 2020). Yet, it is well known that this approach produces inherently biased estimates, particularly for the up component (Brouwer and Hanssen, 2023b). An alternative option is to use the null-line aligned (NLA) coordinate system as proposed in Brouwer and Hanssen (2023b), which ensures unbiased estimates, but produces results that can be more challenging to interpret for non-experts.

Here we demonstrate a practical, effective, and largely generic solution to the underdeterminancy problem, introducing the 'strapdown' method, which uses a location-dependent local reference system that is tuned to the deformation phenomenon. In fact, special cases of this approach have been applied in particular applications, such as landslides (Mohr, 1997; Colesanti and Wasowski, 2006; Notti et al., 2014; Cascini et al., 2010; Greif and Vlcko, 2012; Van Natijne et al., 2022), ice sheets (Joughin et al., 1998; Mattar et al., 1998; Mohr et al., 1998; Ford et al., 2003), and line-infrastructure (Chang et al., 2018; Özer et al., 2019). Yet, apart from being a wider generalization and a mathematical framework, the strapdown approach offers complete error propagation and therefore a proper quality description of the final estimated displacements. Moreover, effectively it leads to an optimal unbiased solution which is locally two-dimensional, but globally three-dimensional, requiring only a limited degree of rather undisputed contextual information on the expected deformation phenomena.

We first discuss the geometry of the strapdown approach and the deformation phenomena for which it can be used. In Sec. 3 we discuss how the displacements can be estimated and we elaborate on the quality of the estimated displacements. Finally, we demonstrate the strapdown approach in two examples in Sec. 4 and reflect on the method in Sec. 5.

2 System Geometry

The geometry of the strapdown system is defined and subsequently elaborated for different classes of deformation phenomena.

2.1 The local strapdown coordinate system

Instead of choosing one coordinate system for the entire area of interest, we define a local, right-handed Cartesian coordinate system that is fixed to the local deformation phenomenon with transversal, longitudinal, and normal (TLN) components, $d_{\mathrm{TLN}} = [d_T, d_L, d_N]^T$, see Fig. 1. The term *local* implies that the orientation of the TLN frame will differ for each location, hence the term '*strapdown*', adapted from inertial navigation technology (Titterton et al., 2004). Thus, a displacement vector d_{TLN} is projected onto the LoS with Eq. (1) as (Chang et al., 2018):

$$d_{\mathrm{LoS}} = P_{\mathrm{LoS}^\perp} R_1 R_2 R_3 d_{\mathrm{TLN}}, = P^R_{\mathrm{LoS}^\perp} d_{\mathrm{TLN}}, \tag{2}$$

neous) displacement velocity, in [mm/y], since this is geometry-invariant.

where R_1, R_2, and R_3 are rotation matrices:

$$R_1 = \begin{bmatrix} \cos\Lambda & \sin\Lambda & 0 \\ -\sin\Lambda & \cos\Lambda & 0 \\ 0 & 0 & 1 \end{bmatrix}, \quad (3)$$

$$R_2 = \begin{bmatrix} 1 & 0 & 0 \\ 0 & \cos\Phi & -\sin\Phi \\ 0 & \sin\Phi & \cos\Phi \end{bmatrix}, \quad (4)$$

$$R_3 = \begin{bmatrix} \cos\Omega & 0 & \sin\Omega \\ 0 & 1 & 0 \\ -\sin\Omega & 0 & \cos\Omega \end{bmatrix}, \quad (5)$$

where $\Lambda \in [0°, 360°)$ is the azimuth of the longitudinal direction (L) relative to the north[2]. The elevation angle of the longitudinal direction is $\Phi \in (-90°, +90°]$, relative to the horizontal[3], and the elevation angle of the transversal direction (T) is $\Omega \in (0°, +90°]$. The normal direction (N) completes the orthogonal right-handed TLN system. $P^R_{\mathrm{LoS}^\perp}$ is the projector that projects the displacement vector d_{TLN} onto the LoS along a plane orthogonal to the LoS. Thus, $P^R_{\mathrm{LoS}^\perp}$ is a function of Λ, Ω, and Φ with size 1×3, i.e., $P^R_{\mathrm{LoS}^\perp} = [P_T, P_L, P_N]$, see App. A.

Geometrically, any displacement vector can be regarded as being situated in a 2D plane, with zero-displacement in the complementary direction, by definition. In the TLN frame, the displacement vector is always situated in the plane spanned by the transversal and normal unit vectors, and is therefore by definition zero in the longitudinal direction. Note that this is not an assumption or an approximation, as it follows deductively from the definition of the coordinate system. Of all 2D planes that contain the displacement vector as subset, there is typically only one plane orientation that is physically genuinely relevant, i.e., uniquely interpretable. This is due to the fact that all observable displacements are relative changes in velocity (Huygens, 1656), which are necessarily a consequence of the sum of all forces acting upon the object (Newton, 1687). Obviously, the force of gravity is omnipresent in every case, and is in many cases also the root cause of the observed motion. In other cases, forces are due to kinetic causes, such as imposed by traffic or due to, e.g., volumetric or tectonic mechanisms (Yu et al., 2013; Cavalié and Jónsson, 2014). Almost without exception, displacement mechanisms of interest have a physical context that can be regarded as 'known' to some extent. Consequently, we can orient the TLN system, viz. the longitudinal direction, to the direction in which there is physically no displacement to be expected, as we will elaborate below. From orthogonality, the longitudinal direction defines the local *displacement plane*, in which the two orthogonal displacement components (T and N) are situated. With this definition, Eq. (2) can be locally solved with LoS observations from two sufficiently different viewing geometries. Consequently, the main challenge is (i) to find the orientation of the local displacement plane in 3D space, given by (Λ, Φ, Ω) and (ii) to approximate the precision of these orientation parameters in order to perform an error propagation to assess the final quality of the local solution.

[2] Due to the 180° ambiguity in longitudinal direction, in case of a topographic slope or a subsidence slope, the longitudinal axis is defined tangential to the local iso-elevation or iso-deformation lines, such that the positive transversal direction is always directed down-slope. In the absence of a clear slope, we use the smallest angle w.r.t. the north, i.e. $\Lambda \in (-90°, +90°]$, following Chang et al. (2018).

[3] where up-hill is positive.

2.2 Deformation phenomena

The generic description of the methodology can be elaborated for typical classes of Lagrangian deformation phenomena (Brouwer and Hanssen, 2023a). Here we discuss downslope displacements, subsidence and uplift, (line)-infrastructure, and motion associated with faults.

2.2.1 Gravity-driven downslope deformation

Landslides, moving glaciers, or slope instabilities of a dike are examples of phenomena where the main deformation occurs along the slope,

with gravity as the main driving force, see Fig. 1. When the longitudinal axis is parallel to the iso-elevation lines of the slope of the occurring landslide, there are no forces in the longitudinal direction, and therefore $d_L = 0$. Hence, all displacements occur in the (vertical) plane spanned by the transversal and normal axis, shown in the side views of Fig. 1, and $\Phi = 0°$ by definition, see Eq. (5). The slope *aspect*, α_a, i.e., the compass direction that a terrain surface faces, determines the value for the angle Λ since the (angle of the) slope, Ω, is always referred to as a positive number, see Fig. 1, i.e., $\alpha_a = \Lambda + 90°$. The positive transversal direction is always directed down-slope.

2.2.2 Subsidence and uplift

Subsidence bowls and uplift domes are caused by a subsurface volume change, in combination with gravity, see the sketch in Fig. 1. They exhibit vertical and horizontal displacement components (Kratzsch, 1983). The horizontal displacements are centripetal for subsidence, and centrifugal for uplift (Müller and Preusse, 2018). Thus, the longitudinal direction, indicated by azimuth Λ, is oriented parallel to the iso-deformation lines, and the transversal direction is downslope (centripetal) for subsidence, and centrifugal for uplift. Similar to the downslope case, there is—by definition—no displacement component in the longitudinal direction. The normal displacements are maximum in the center of the field, decreasing asymptotically to the edge of the field. The example in section 4.1 elaborates this further.

2.2.3 Line-infrastructure

Line infrastructure assets are characterized by an extended spatial dimension in one direction (by definition the longitudinal direction), where the spatial extent in the other two directions is limited, such as roads, railways, dikes, and pipelines. The slope of the asset is given by Φ, while Ω represents the cant of the asset or the slope in the transversal direction (Chang et al., 2014, 2018). The latter is usually small, see Fig. 2. Often, it is possible to assume that no significant continuous (stationary) displacements occur in the longitudinal direction (Chang et al., 2014, 2018; Özer et al., 2019), apart from perhaps thermal expansion and contraction which can be independently modeled and has a non-secular character.

2.2.4 Motion associated with faults

Although deformations resulting from tectonics (post, co-, and inter-seismic) are often too complex to uniquely identify the 2D plane in which the displacements occur, we can still utilize the strapdown method for deformations associated with faults, e.g., in relation to hydrological effects. In such cases the driver of the deformation is sufficiently well defined and determines its directionality. Considering, e.g., rising mine water associated with normal or reverse faults (Caro Cuenca et al., 2013), see Fig. 3. In such cases, no displacements are expected along the fault and the longitudinal direction can thus be directed parallel to the fault. In section 4.2 this example is further elaborated. For ideal strike-slip faults, the sides move along each other and the longitudinal direction is directed perpendicular to the fault. To prevent directional ambiguity, the smallest azimuth angle is chosen, i.e., $\Lambda \in (-90°, 90°]$. Note that for all three fundamental fault types, d_T has a different sign at both sides of the fault.

3 Estimating displacements using the strapdown approach

As longitudinal displacements are null by definition, any displacement vector can be unambiguously represented in a 2D (d_T, d_N) system, and thus d_T and d_N can be estimated with two LoS observations. There are several options for estimating d_T and d_N. Chang et al. (2014, 2018) add a pseudo observation, $d_L = 0$, to the mathematical model. However, this approach requires the orientation of the TLN frame to

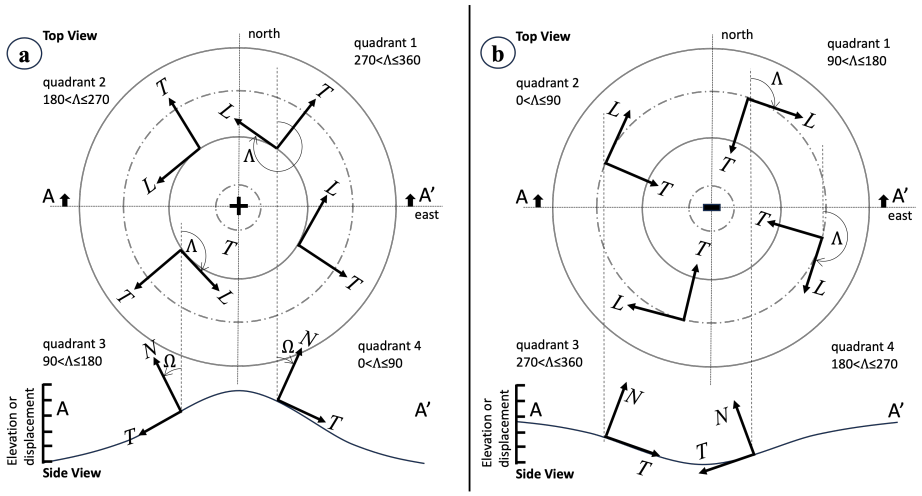

Fig. 1 The orientation of the TLN reference system for gravity-induced downslope deformation phenomena and/or subsidence and uplift. (a) shows the orientation for a schematized mountain (with iso-elevation lines) or an uplift dome (with iso-displacement lines). Note that the transversal direction is always downslope or centrifugal. Therefore, the slope aspect determines the boundaries within which Λ should lie. (b) Similar situation sketch for a valley or subsidence bowl. Note that the transversal axis is always downslope, and thus centripetal for subsidence.

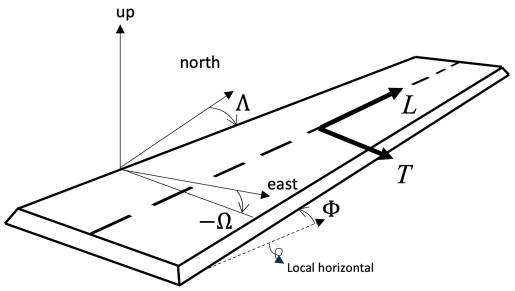

Fig. 2 The orientation of the TLN reference system for line-infrastructure: Φ represents the slope in the longitudinal direction and Ω the cant. Figure adapted from Chang et al. (2014).

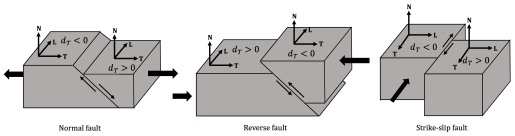

Fig. 3 Orientation of the TLN reference frame for the fundamental types of fault motion (Fowler, 1990). For normal and reverse faults, no displacements are expected along the fault, aligning the longitudinal direction is parallel to the fault. For strike-slip faults the displacements happen mainly along the slope, aligning the longitudinal direction perpendicular to the fault.

be perfectly known, since a misalignment will result in biased estimates for d_T and d_N.[4] The orientation of the TN plane will always have some alignment uncertainty, expressed by σ^2_Λ, σ^2_Ω, and σ^2_Φ. A better alignment precision results in a better estimation of the unknown displacements d_T and d_N. Below, we consider the impact of the alignment uncertainty in the mathematical model.

3.1 The mathematical model

Since the longitudinal displacements are null by definition, d_L can be removed from Eq. (2) and $P^R_{\mathrm{LoS}^\perp}$ reduces to a 1×2 matrix with only P_T and P_N, see App. A, and the 2×1 displacement vector contains only d_T and d_N. The TLN frame orientation is introduced using pseudo observations $\underline{\Lambda}$, $\underline{\Omega}$, and $\underline{\Phi}$ (the underline indicates the stochastic nature of the

[4] Adding pseudo observation $d_L = 0$ to the system of equations, while in fact $d_L \neq 0$, results in a 'decomposition error' similar to 'neglecting' the north component in a conventional ENU decomposition, see Brouwer and Hanssen (2023b).

observable) in the mathematical model:

$$E\{\underbrace{\begin{bmatrix} \underline{d}^{(1)}_{\mathrm{LoS}} \\ \vdots \\ \underline{d}^{(m)}_{\mathrm{LoS}} \\ \underline{\Lambda} \\ \underline{\Omega} \\ \underline{\Phi} \end{bmatrix}}_{y}\} = \underbrace{\begin{bmatrix} a_1(x) \\ \vdots \\ a_m(x) \\ a_{m+1}(x) \\ a_{m+2}(x) \\ a_{m+3}(x) \end{bmatrix}}_{A(x)}, \text{ and} \tag{6}$$

$$D\{\underbrace{\begin{bmatrix} \underline{d}^{(1)}_{\mathrm{LoS}} \\ \vdots \\ \underline{d}^{(m)}_{\mathrm{LoS}} \\ \underline{\Lambda} \\ \underline{\Omega} \\ \underline{\Phi} \end{bmatrix}}_{y}\} = \underbrace{\begin{bmatrix} Q_{\mathrm{LoS},1} & \dots & 0 & 0 & 0 & 0 \\ \vdots & \ddots & \vdots & 0 & 0 & 0 \\ 0 & \dots & Q_{\mathrm{LoS},m} & 0 & 0 & 0 \\ 0 & 0 & 0 & \sigma^2_{\Lambda} & 0 & 0 \\ 0 & 0 & 0 & 0 & \sigma^2_{\Omega} & 0 \\ 0 & 0 & 0 & 0 & 0 & \sigma^2_{\Phi} \end{bmatrix}}_{Q_{yy}}, \tag{7}$$

where for $i \in [1, m]$

$$\begin{aligned} a_i(x) &= P^{(i)}_T(\Lambda, \Omega, \Phi)d_T + P^{(i)}_N(\Lambda, \Omega, \Phi)d_N \\ a_{m+1}(x) &= \Lambda \\ a_{m+2}(x) &= \Omega \\ a_{m+3}(x) &= \Phi, \end{aligned}$$

and $x = [d_T, d_N, \Lambda, \Omega, \Phi]^T$ is the vector of unknown displacements and orientation angles. $E\{.\}$ expresses the expectation of the model, which can be solved with two sets, i.e., $m = 2$, of LoS observations: $\underline{d}^{(1)}_{\mathrm{LoS}}$ and $\underline{d}^{(2)}_{\mathrm{LoS}}$, each having a different viewing geometry.[5] Note that the size of each set can be be different due to a different number of available scatterers. Rows $i \in [1, m]$ in the A matrix are non-linear equations of x, where each row is unique due to the difference in viewing geometry. To overcome the rank deficiency, pseudo observations for $\underline{\Lambda}$, $\underline{\Omega}$, and $\underline{\Phi}$ are added based on a best-effort approximation.[6] $D\{.\}$ is the dispersion of the model, where $Q_{\mathrm{LoS},i}$ is the covariance matrix of the LoS observations for set i. This covariance matrix is a diagonal matrix containing the variances of displacements for each scatterer within the set. The uncertainty in our best-effort attempt to orient the TLN frame is quantified in σ^2_{Λ}, σ^2_{Ω}, and σ^2_{Φ}. Since the model is non-linear, the solution can be found by using a Gauss-Newton iteration process.

[5] For a successful estimation of x, the two LoS observations 'sets' need to be spatio-temporally coinciding and independent (STCI). As this is hardly ever possible, a region of uniform motion (RUM) needs to be defined and a datum connection (in time and space) needs to be performed. Moreover, the two LoS observation sets need to have a sufficient angular diversity. For in-depth elaboration see Brouwer and Hanssen (2023b).

[6] The best-effort frame orientation approximation can be purely data-driven based on iso-displacement lines retrieved from the original line-of-sight results, or on contextual information, as long as conservative precision estimates are used.

3.1.1 Gauss-Newton Iteration

To estimate the five unknown parameters, the linearized system of equations needs to be solved,

$$\Delta\underline{y}_{[0]} \approx J_{[0]}\Delta x_{[0]}, \tag{8}$$

where

$$J_{[0]} = \begin{bmatrix} \frac{\partial}{\partial d_T}a_1(x_{[0]}) & \dots & \frac{\partial}{\partial \Phi}a_1(x_{[0]}) \\ \vdots & \vdots & \vdots \\ \frac{\partial}{\partial d_T}a_{m+3}(x_{[0]}) & \dots & \frac{\partial}{\partial \Phi}a_{m+3}(x_{[0]}) \end{bmatrix} \tag{9}$$

is the Jacobian matrix which is a function of the initial approximations for the unknown parameters $x_{[0]}$, i.e.,

$$x_{[0]} = \left[d_{T_{[0]}}, d_{N_{[0]}}, \Lambda_{[0]}, \Omega_{[0]}, \Phi_{[0]}\right]^T, \tag{10}$$

which yield initial approximations for the observation vector $\underline{y}$ and $\Delta\underline{y}_{[0]} = \underline{y} - A(x_{[0]})$. Consequently, when $m \geq 2$, Δx can be estimated using direct inversion or Best Linear Unbiased Estimation (BLUE) (Teunissen, 2003), i.e.,

$$\Delta\underline{\hat{x}}_{[0]} = \begin{cases} J^{-1}_{[0]}\Delta\underline{y}_{[0]}, & \text{for } m = 2, \text{ and} \\ Q_{\hat{x}\hat{x}}J^T_{[0]}Q^{-1}_{yy}\Delta\underline{y}_{[0]} & \text{for } m > 2, \end{cases} \tag{11}$$

$$Q_{\hat{x}\hat{x}} = \begin{cases} J^{-1}_{[0]}Q^{-1}_{yy}J^{-1}_{[0]}, & \text{for } m = 2, \text{ and} \\ \left(J^T_{[0]}Q^{-1}_{yy}J_{[0]}\right)^{-1} & \text{for } m > 2, \end{cases} \tag{12}$$

where $Q_{\hat{x}\hat{x}}$ represents the precision of x. The new estimate for $\underline{\hat{x}}$ is defined as $\underline{\hat{x}}_{[1]} = x_{[0]} + \Delta\underline{\hat{x}}_{[0]}$, and can be used to estimate $\Delta x_{[1]}$. Iteration leads to a final estimate for $\underline{\hat{x}}$. An estimation of the unknown parameters requires rough initial approximations for which either prior knowledge of the deformation phenomenon can be used, or initial assessments from the original LoS estimates. For $\Lambda_{[0]}$, $\Omega_{[0]}$, and $\Phi_{[0]}$ the best-effort frame orientations are used.

The precision of the five estimated parameters is expressed by the (co)variances in $Q_{\hat{x}\hat{x}}$, sketched for an arbitrary frame orientation in Fig. 4. There is correlation between d_T and d_N,

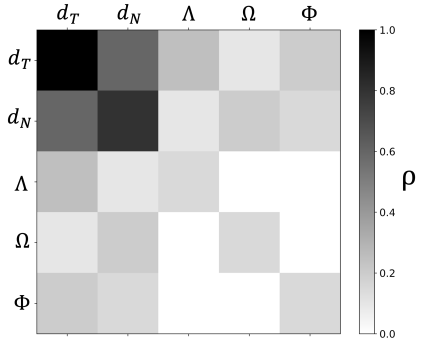

Fig. 4 Sketch of (normalized) $Q_{\hat{x}\hat{x}}$ for an arbitrary frame orientation. The diagonal elements represent the precision of the estimated parameters $\hat{x}$ and the off-diagonal terms the correlation between them. There is correlation between the estimated displacements (upper-left 2×2 block) but no correlation between the estimated frame orientation (lower-right 3×3 block). There is correlation between the estimates for the frame orientation and for the displacements.

in the upper 2×2 block. Due to the choice of the pseudo-observations, there is no correlation between the estimated orientation angles Λ, Ω and Φ. Yet, there is correlation between the displacement and the angular estimates. Different frame orientations will result in different levels of correlation.

3.2 The quality of the estimates

The precision of the estimates $(\underline{\hat{d}}_T, \underline{\hat{d}}_N)$ depends on four independent contributions: (i) the actual (true) orientation of the TLN frame, (ii) the actual (true) magnitude of the d_T and d_N displacements, (iii) the alignment precision of the TLN frame, and (iv) the precision of the observations and pseudo-observations. These will be discussed below.

3.2.1 True orientation of the TLN frame

The actual (true) orientation of the TLN frame has a dominant impact on the precision of the final estimates. With two LoS observation geometries (ascending and descending), displacement components in the direction of the *null-line* (Brouwer and Hanssen, 2023b) cannot be observed: the more either the transversal or normal direction aligns with of the null-line, the less precise that parameter can be estimated. The most favourable option is therefore when the plane spanned by the transversal and normal axis (TN-plane) is orthogonal to the null-line, i.e., when $\Lambda = \phi$ and $\Phi = \zeta$, where ϕ and ζ are the azimuth angle and elevation angle of the null-line, respectively.[7]

Fig. 5 shows the Signal-to-Noise Ratio (SNR) for the transversal (lower left) and normal (upper left) component as a function of Λ and Ω, with $\Phi = 0°$. We simulate an arbitrary displacement phenomenon with $d_T = d_N$, observed from an ascending and a descending orbit with viewing characteristics as presented in Tab. 1. For different frame orientations, we simulate LoS observations and subsequently estimate the unknown parameters x with Eq. (11). In Fig. 5, we show the SNR for each realization, where $\mathrm{SNR}_T = 10\log_{10}(d_T/\sigma_{d_T})$, and $\mathrm{SNR}_N = 10\log_{10}(d_N/\sigma_{d_N})$ represent the transversal and normal direction respectively, shown by the two left figures. The quality of the estimated normal component is best when the

[7] In this special case the TLN frame is identical to the null-line aligned (NLA) frame, see Brouwer and Hanssen (2023b) .

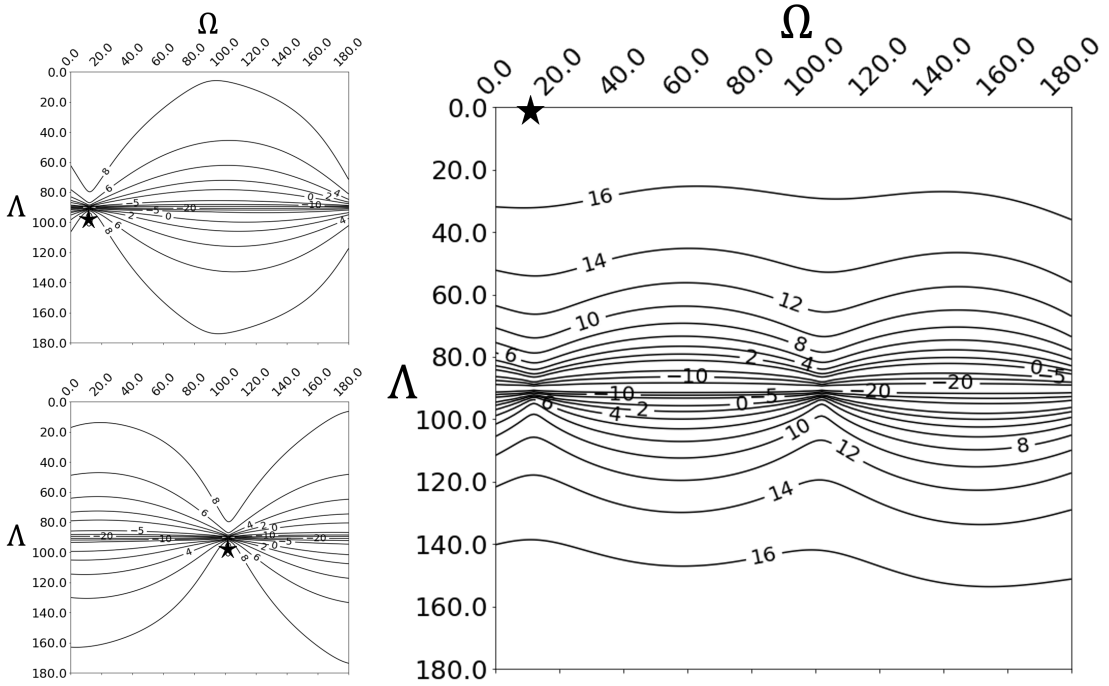

Fig. 5 SNR [dB] for the normal (upper left) and transversal (lower left) component for different orientations of the TLN frame. The observation geometry of the simulated ascending and descending acquisition is presented in Tab. 1, which result in a null-line orientation, $n(\phi, \zeta) = n(0.14°, 12.14°)$. The right figure shows the sum of the left two figures since one is always interested in estimating both components. It can be seen that the SNR of the two combined directions is greatest when the longitudinal direction is in the direction of the null-line, indicated by the black star. In that specific case, the TN plane is orthogonal to the null-line.

Table 1 Simulated viewing geometries and consequent null-line orientation.

Geometry	Inc. angle θ	Azim. ZDP α_d
ascending	32°	250°
descending	40°	105°
null-line n:	$\phi = 0.14°$	$\zeta = 12.14°$

transversal direction aligns with the null-line, shown by the black star in Fig. 5. Likewise, the quality for d_t is the best when the normal direction aligns with the null-line. Obviously, when one of the two components aligns with the null-line, both satellite acquisitions have zero sensitivity in that direction, and both observations are entirely attributed to the other component.

In reality, we need to estimate *both* components in concert. Therefore we show the sum of the SNR ratios in the right figure, i.e., $\mathrm{SNR}_{\mathrm{total}} = \mathrm{SNR}_N + \mathrm{SNR}_T$. The black star shows the most favourable orientation with the highest SNR value, which occurs when the longitudinal direction is aligned with the null-line, e.g., $\Lambda = \phi$ and $\Omega = \zeta$. The quality of the estimates is poor when $\Lambda \approx 90°$, i.e., when the normal or transversal direction is in the direction of the null-line.

3.2.2 True magnitude of d_T and d_N

The quality (both bias and precision) of $(\underline{\hat{d}}_T, \underline{\hat{d}}_N)$ is scaled by the actual (but unknown) size of the displacement signal. This follows from the Jacobian in Eq. (9), which requires approximations $d_{T_{[0]}}$ and $d_{N_{[0]}}$.

3.2.3 Alignment precision of the TLN frame

Any error in the best-effort orientation approximation of the TLN frame, i.e., a misalignment, results in $d_L \neq 0$, and consequently biased estimates for d_T and d_N. Misalignments are taken into account in Eqs. (6) and (7), via σ_Λ, σ_Ω, and σ_Φ, propagating the alignment uncertainty to the precision for the final estimates, see Eq. (12). The alignment precision needs to be chosen conservatively, i.e., not too optimistic, such that the (potential) bias in $\hat{\underline{d}}_T$ and $\hat{\underline{d}}_N$ will fall within the confidence bounds of the estimator.

3.2.4 Precision of (pseudo) observations

The fourth contribution to the precision of the estimates $(\hat{\underline{d}}_T, \hat{\underline{d}}_N)$ is the quality (or precision) of (i) the LoS observations and (ii) the pseudo-observations, expressed in Q_{yy} in Eq. (12). A higher quality of the observations, and/or more certainty in the frame orientation, results via $Q_{\hat{x}\hat{x}}$ in higher quality final estimates.

3.3 Interpretation of the results

For a cartographic uniform visualization of the estimated (d_T, d_N) displacements there are two options. When the orientation of the strapdown coordinate system is uniform over the area of interest, it is possible to create a panchromatic map[8] for d_T and d_N separately, see, e.g., Figs. 11e and f. However, in the more generic case of a spatially variable orientation of the strapdown coordinate system this is not possible anymore, since directionality needs to be considered. A *vector* (quiver) map type is more suitable in this case, see Figs. 6 and 8. This has the added value that the precision of both magnitude and direction can be expressed using a confidence ellipse. The relative sizes of the vector and the confidence ellipse enable a direct assessment of the significance of the estimate and of the SNR, and hence improve interpretability. In Fig. 6, the estimated transversal displacement vector d_T, located at the geometric center of a RUM, [9] is situated at geographic coordinates (x_i, y_i). In this case the normal direction is practically aligned with the up direction.[10] The error ellipse shows the confidence region, with transversal axis $p\,\sigma_T$, and longitudinal axis $\sigma_L = d_T \tan(p\,\sigma_\Lambda)$ where p expresses the desired size of the confidence region, i.e., for $p = 2$ we have a 95% confidence region. Both σ_T and σ_Λ follow from Eq. (12).

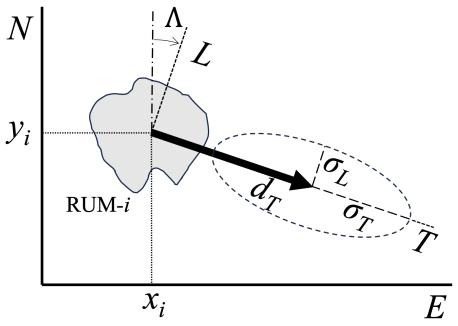

Fig. 6 Vector representation of strapdown results of RUM-i at geographic coordinates (x_i, y_i), showing the estimated transversal displacement component, d_T. The error ellipse or confidence region has two axes. The size of transversal axis is σ_T and the size of the longitudinal axis is $\sigma_L = d_T \tan \sigma_\Lambda$.

4 Results: 2 case studies

In this section we apply the strapdown approach on two case studies: subsidence due to solution mining and displacements resulting from ground water pressure in relation to faults.

4.1 Magnesium extraction in Veendam

In Veendam, the Netherlands, solution mining for multicomponent salts occurs at a depth of

[8] or similarly a contour map or a dot distribution map.

[9] region of uniform motion, see Brouwer and Hanssen (2023b).

[10] In other cases, the displacement vector can be situated along the slope.

Table 2 Acquisition details for Sentinel-1 tracks 15 and 139 at Veendam, the Netherlands.

	S1 track 15	S1 track 139
Heading	ascending	descending
Mean θ	36.3°	44.2°
Mean α_d	261°	98°
Start	Aug 7, 2018	Aug 4, 2018
End	Mar 8, 2020	Feb 16, 2020

∼1500 m. Around the production caverns, salt starts flowing towards the caverns (Brinkman, 2016). Subsequently, the overlaying rock layers move downwards and horizontally towards the center of the cavern, resulting in a subsidence bowl. The observed vertical displacements will be greatest at the center of the bowl, while the horizontal displacements are centripetal, see Sec. 2.2.2. We use the strapdown approach to estimate the unknown 3D displacements. The area is monitored by Sentinel-1 from descending and ascending acquisitions, see Tab. 2, using a PSI approach (van Leijen, 2014). The LoS results for both geometries are shown in Fig. 8. For the descending acquisition, the greatest LoS velocities occur more to the east compared to the ascending acquisition, which is an indicator for significant horizontal displacements.

4.1.1 RUM definition

As the orientation of the TLN frame varies within the region, in first iteration we approximate the subsidence bowl assuming radial symmetry and divide it into 12 sectors and five equidistant radial areas, see Fig. 8, where each element is assumed to behave as a region of uniform motion (RUM). To account for imperfect circularity we set $\sigma_\Lambda = 5°$, implying that, with a 95% confidence interval, we conservatively estimate the Λ^0 alignment to be within $\pm 10°$. We use $\Omega^0 = 0°$ and $\Phi^0 = 0°$ due to the absence of significant topography, and we set $\sigma_\Omega = 2°$ and $\sigma_\Phi = 2°$, to quantify our confidence in this assumption.

4.1.2 Parameter estimation per RUM

Independently for each RUM we estimate the mean LoS displacement velocity for each viewing geometry, i.e., $\hat{v}_{\text{LoS}}^{\text{asc}}$ and $\hat{v}_{\text{LoS}}^{\text{dsc}}$, based on all time series of the scatterers within that particular RUM. Subsequently, we estimate the average velocities in the transversal and normal direction, $\hat{v}_T$ and $\hat{v}_N$, with Eqs. (6) and (7), see Fig. 8. The largest mean normal (near-vertical) displacement of ∼40 mm/y indeed occurs at the center of the subsidence bowl. RUMs A4, A6, A7, and A8 contain only scatterers in one viewing geometry, impeding strapdown estimates.

We estimate the precision for the unknown velocities, $Q_{\hat{x}\hat{x}}$, visualized by 2σ confidence ellipses and error bars for the normal velocities. The minor axes of the ellipses represent the level of confidence due to the uncertainty in the alignment of the frame. The uncertainty of both the transversal and the normal velocity differs per RUM. Since the orientation of the null-line is near-north ($\phi = 0.7°$ and $\zeta = 7.1°$), the transversal direction is almost in the direction of the null-line for RUMs 1, 12, 6, and 7, which is properly addressed by the confidence regions for these regions. It can be seen that also the normal component is affected.

For comparison, the conventional biased approach is followed where the north component is neglected and only the east and up components are estimated, leading to a decomposition error (Brouwer and Hanssen, 2023b). In Fig. 9, we show the biased estimated east and up components using that approach. The comparison shows that the strapdown approach captures the entire 3D deformation phenomenon: while we estimate 2D displacements per RUM, we retrieve the full 3D displacement phenomenon by combining all RUMs, hence the *'2D-local, 3D-global'* characterization. In Fig. 10, we show the difference in estimated velocity between the up component from the east-up approach and the normal component in the strapdown approach. The greatest errors, up to −5.4 mm/y,

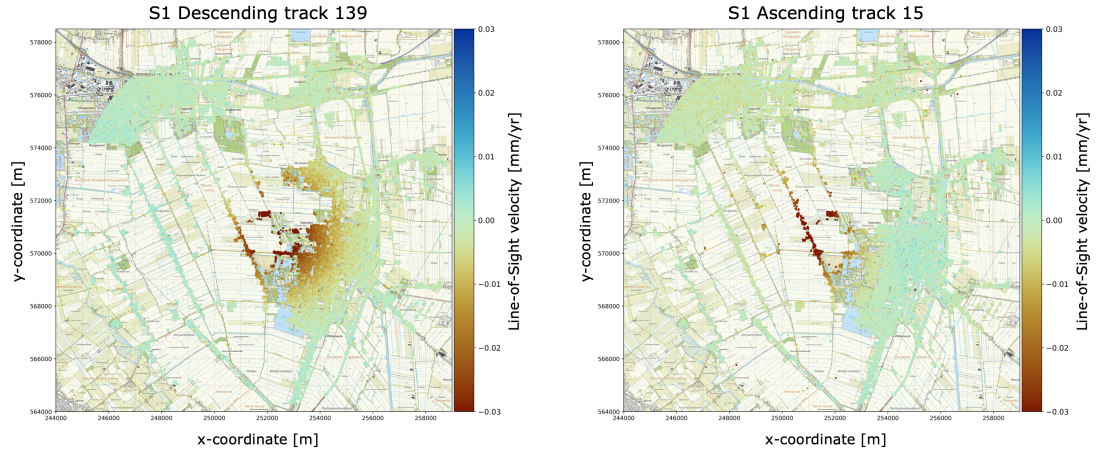

Fig. 7 Estimated LoS velocities for S1 descending track 139 and ascending track 15 for Veendam. The location of the maximum LoS velocity differs for both tracks. This is an early indicator for significant horizontal displacements.

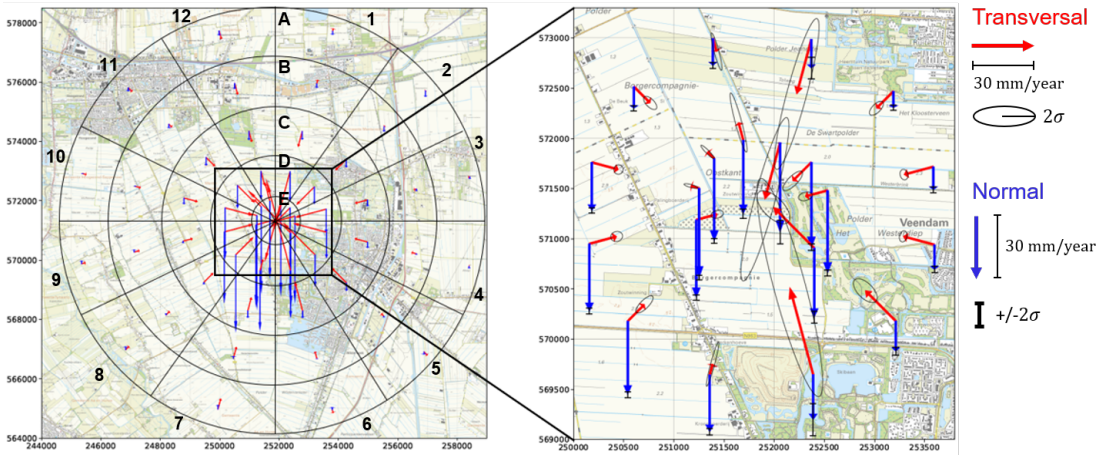

Fig. 8 Results for strapdown approach at a subsidence bowl which is the result of magnesium extraction at Veendam. The red arrows represent the estimated displacement velocity vectors in the transversal direction (near-horizontal), and their 2σ uncertainty is visualized by a 95% confidence ellipse. The blue arrows are the displacement velocities in the normal direction (near-vertical), which have a $\pm 2\sigma$ error bar.

occur in RUMs located in the north and south, due to the large neglected north component.

In comparison, the neglect-north approach results in (i) no information on the north component at all (even if it would be significant enough to be estimated reliably), and (ii) less accurate (i.e., biased) estimates in the east and north components. The strapdown approach leads to three-dimensional unbiased (east-north-up) estimates, accompanied with realistic precision metrics that enable realistic interpretation.

4.2 Coal mining after-effects

From 1900 until 1970, coal was extracted from mines in Limburg, the Netherlands (Van Bergen et al., 2007). One of its after-effects is differential ground heave induced by rising mine water (Pöttgens, 1985; Caro Cuenca et al., 2013).

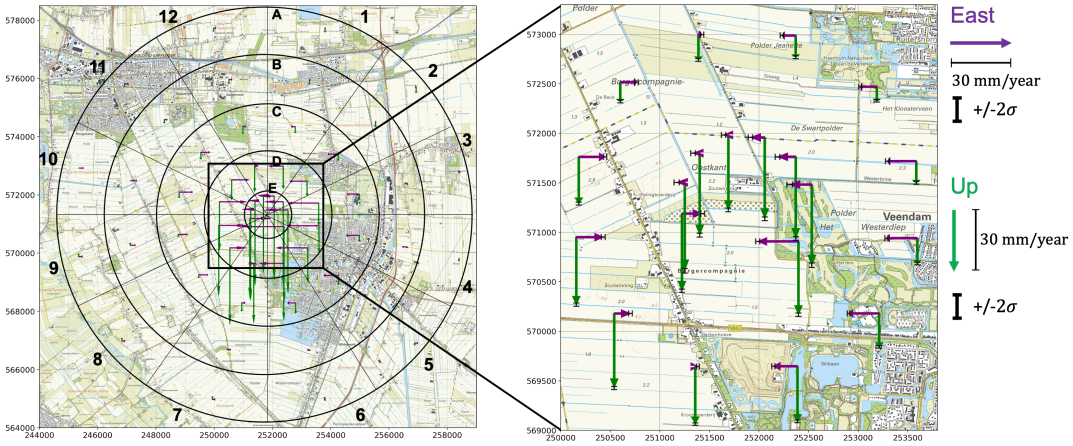

Fig. 9 Estimated East and Up displacements while neglecting the North component for Veendam. Note that this is a decomposition error and result in biased estimates, especially for the Up component.

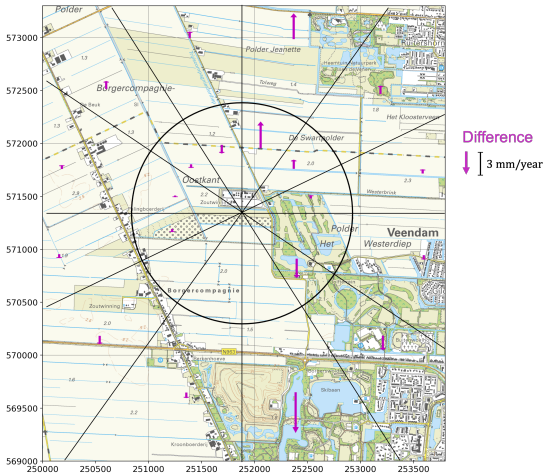

Fig. 10 The difference between the estimated Up and transversal component. If the arrow for a RUM points up, it means that the estimated Up component is smaller than the estimated transversal component. The Up component is thus an under estimation of the actual vertical displacement.

Three major ground heave zones are known, one of which is situated near Brunssum along the Feldbiss fault (Heitfeld and Klunker, 2016). Here we investigate the displacements near this fault.

Table 3 Acquisition details Radarsat-2

	track 109	track 302
Heading	ascending	descending
Mean θ	37.3°	33.4°
Mean α_d	259.2°	100.9°
Start	Dec 14, 2016	Dec 4, 2016
End	Sep 12, 2020	Sep 26, 2020

4.2.1 Deformation phenomenon and RUMs

The Brunssum area is monitored by Radarsat-2 from an ascending and a descending geometry, see Tab. 3. Differential displacements are estimated using a PSI approach, for both geometries independently (van Leijen, 2014). The LoS displacement rate estimates are projected onto

the vertical (PoV) (Brouwer and Hanssen, 2023b), see Figs. 11a and b. Close to the Feldbiss fault, the two acquisition geometries clearly show different results, which is an indication for significant horizontal displacement components.

For comparison, we estimate the conventional up ('vertical') and east velocities, by neglecting the north-bound displacement components, resulting in biased estimates, see Brouwer and Hanssen (2023b). The resulting vertical and east displacement rates are presented in Figs. 11c and d, respectively. They suggest that the area is moving upward at the southwest side of the fault, while at the northeast side, the vertical displacements seem minimal. The estimated east displacement rates, Fig. 11d, are difficult to interpret, since they underestimate the real horizontal displacement rates.

From the LoS displacement estimates we hypothesize that the surface movement is correlated with the orientation of the Feldbiss fault, and that the horizontal displacements are directed orthogonal to it, as the driving mechanism is most likely related to the redistribution of subsurface water pressure. There is no physical indication to assume a strike-slip component (parallel to the fault direction) in this case.

Therefore, we use the strapdown approach where for each RUM the longitudinal axis is defined parallel to the Feldbiss fault. We divide the area into grid cells of ∼70×70 m.

4.2.2 Parameter estimation per RUM

Per grid cell (RUM), we estimate the mean LoS displacement rate for both the ascending and descending acquisition, and we compute the mean incidence angle and azimuth of the ZDP. Subsequently, we estimate the normal and transversal displacement rates using Eqs. (6) and (7) and estimate the frame orientation parameters to be $\Lambda_{[0]} = -55^\circ$ and $\Omega_{[0]} = \Phi_{[0]} = 0^\circ$, using $\sigma_\Lambda = 10^\circ$ and $\sigma_\Omega = \sigma_\Phi = 5^\circ$ for each grid cell.

The estimated transversal and normal displacement rates per grid cell are shown in Fig. 11e and f. At the southwest, we find positive normal displacements, implying that the area moves relatively upward. A maximum normal velocity of ∼8 mm/y is found at the south. At the northeast, relative normal displacements are near-zero but significant transversal displacements are estimated. Northeast of the fault, we find positive transversal displacements, with a maximum of ∼10 mm/y, while at the southwest of the fault, transversal displacements are negative, meaning that the two sides of the fault move away from each other, i.e., there is extensional strain. Moreover, we find that the largest transversal displacements are ∼6 mm/y. Since the displacement time-series has a length of almost four years, the total displacement is ∼2.3 cm. As the area with the largest transversal displacements has a width of ∼400 m, this results in ∼23 $\mu\varepsilon$ (micro-strain).

Comparing the strapdown with the neglect-north results, we find significant differences, with better displacement estimates (in terms of bias and precision), better alignment with the known fault location, and generally a better physically interpretable result for the strapdown results. The east component clearly underestimates the horizontal displacements compared to the transversal component.

5 Conclusions

The strapdown method makes it possible to estimate three-dimensional displacements from two satellite imaging geometries, using minimal and largely undisputed contextual information. The method uses a local reference system, with displacement occurring only in the transversal-normal plane. Since the orientation of the local frame is based on the physics of the problem at hand, the strapdown approach gives physically more relevant estimates compared to conventional approaches. By quantifying the uncertainty in the knowledge about the orientation of the local frame, proper error propagation enables assessing the quality of the final estimates. In this way, even when the frame orientation is poorly known, it is still

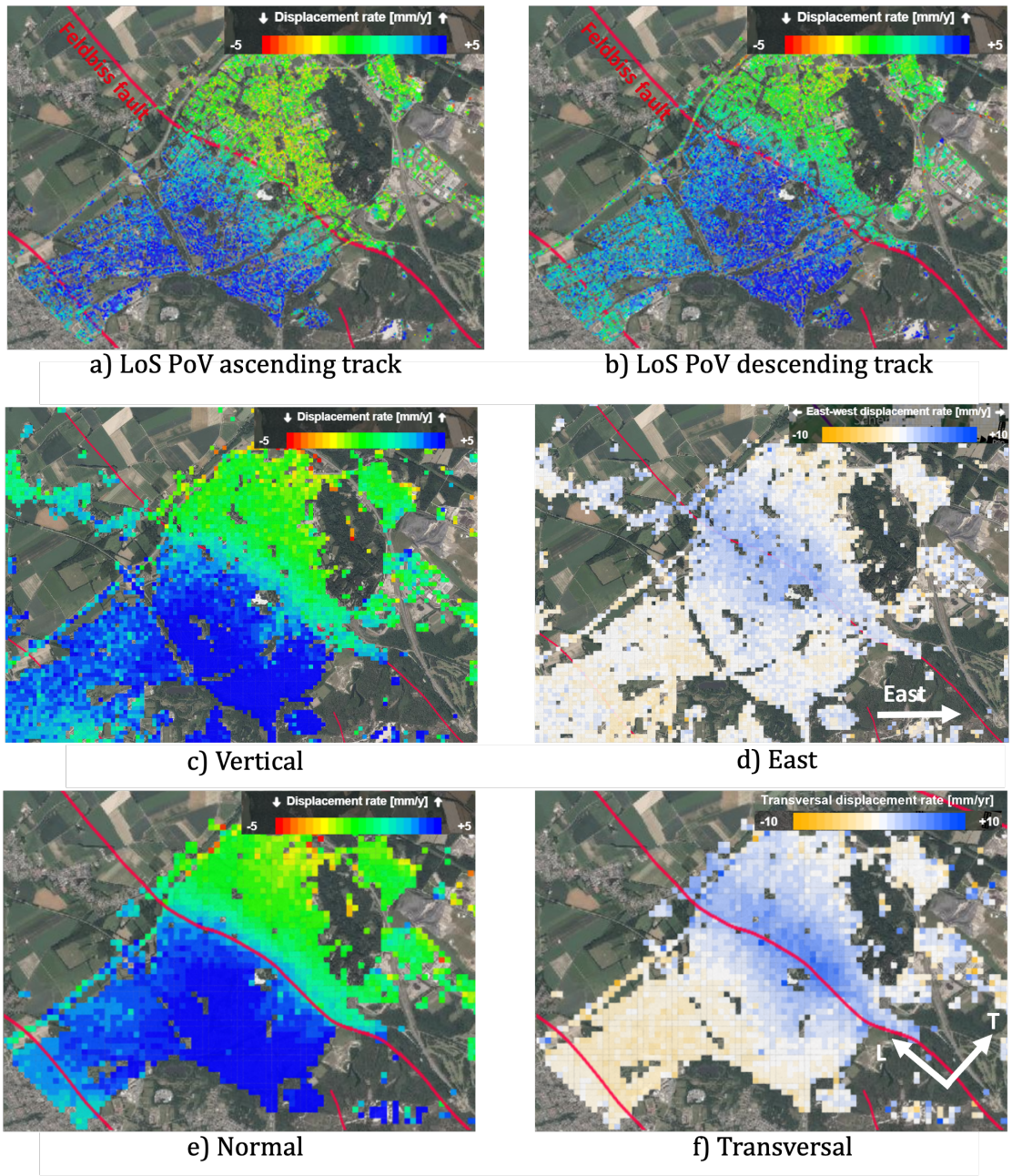

Fig. 11 Estimated displacement rates (mm/y) for the area of Brunssum, the Netherlands. The Feldbiss fault runs trough the middle of the city in the direction NW-SE, indicated by the red line. (a) and (b): LoS displacement rates projected onto the vertical (PoV) for the ascending and descending track respectively. (c) and (d): vertical and east displacement rates, by neglecting the north component. Note that this is decomposition error that typically results in biased estimates (Brouwer and Hanssen, 2023b). Blue and orange values in (d) indicate eastbound and westbound motion, respectively. (e) and (f): normal and transversal displacement rates estimated with the strapdown approach. Blue values in (e) indicate motion in the normal direction, which is upward. Blue and orange values in (f) indicate displacements in the positive and negative transversal direction, respectively.

possible to estimate transversal and normal displacement components, and subsequently the east and north components, as long as the 'true' frame orientation is within the estimated orientation uncertainty. Cartographic representations of the three-dimensional results include the re-introduction of classic geodetic vector-based visualizations, including confidence ellipses, which enables a more profound interpretation of the results.

6 Acknowledgements

We would like to thank SkyGeo for processing and providing the data for the two case studies.

References

Brinkman, J. (2016). *Invloed van bodemdaling door zoutwinning Nedmag op bebouwing*. Deltares report.

Brouwer, W. S. and Hanssen, R. F. (2023a). Classification of geodetic deformation monitoring in Eulerian and Lagrangian frameworks and its consequences for derived products. *Publication in preparation*.

Brouwer, W. S. and Hanssen, R. F. (2023b). A treatise on InSAR geometry and 3D displacement estimation. *IEEE transactions on geoscience and remote sensing*, forthcoming.

Caro Cuenca, M., Hooper, A. J., and Hanssen, R. F. (2013). Surface deformation induced by water influx in the abandoned coal mines in Limburg, The Netherlands observed by satellite radar interferometry. *Journal of Applied Geophysics*, 88:1–11.

Cascini, L., Fornaro, G., and Peduto, D. (2010). Advanced low-and full-resolution dinsar map generation for slow-moving landslide analysis at different scales. *Engineering Geology*, 112(1-4):29–42.

Cavalié, O. and Jónsson, S. (2014). Block-like plate movements in eastern Anatolia observed by InSAR. *Geophysical Research Letters*, 41(1):26–31.

Chang, L., Dollevoet, R., and Hanssen, R. (2014). Railway infrastructure monitoring using satellite radar data. *Int. J. Railw. Technol*, 3:79–91.

Chang, L., Dollevoet, R. P., and Hanssen, R. F. (2018). Monitoring line-infrastructure with multisensor sar interferometry: products and performance assessment metrics. *IEEE journal of selected topics in applied earth observations and remote sensing*, 11(5):1593–1605.

Colesanti, C. and Wasowski, J. (2006). Investigating landslides with space-borne synthetic aperture radar (SAR) interferometry. *Engineering geology*, 88(3-4):173–199.

Crosetto, M., Solari, L., Mróz, M., Balasis-Levinsen, J., Casagli, N., Frei, M., Oyen, A., Moldestad, D. A., Bateson, L., Guerrieri, L., et al. (2020). The evolution of wide-area DInSAR: From regional and national services to the European ground motion service. *Remote Sensing*, 12(12):2043.

Fialko, Y., Sandwell, D., Agnew, D., Simons, M., Shearer, P., and Minster, B. (2002). Deformation on nearby faults induced by the 1999 Hector Mine earthquake. *Science*, 297:1858–1862.

Ford, A. L., Forster, R. R., and Bruhn, R. L. (2003). Ice surface velocity patterns on Seward Glacier, Alaska/Yukon, and their implications for regional tectonics in the Saint Elias Mountains. *Annals of Glaciology*, 36:21–28.

Fowler, C. M. R. (1990). *The solid earth: an introduction to global geophysics*. Cambridge University Press.

Greif, V. and Vlcko, J. (2012). Monitoring of post-failure landslide deformation by the PS-InSAR technique at Lubietova in Central Slovakia. *Environmental Earth Sciences*, 66(6):1585–1595.

Hanssen, R. F. (2001). *Radar interferometry: data interpretation and error analysis*, volume 2. Springer Science & Business Media.

Heitfeld, M. and Klunker, J. e. a. (2016). *Na-ijlende gevolgen steenkolenwinning Zuid-Limburg - Summary report with integrated*

Bow-Tie-Analysis, volume 1. Projectgroep GS-SL.

Huygens, C. (1656). Hug 7 a, ff. 24r-v, inc. motus inter corpora relativus tantum est. *Codices Hugeniani*, (Codex HUG 07 A-018).

Joughin, I. R., Kwok, R., and Fahnestock, M. A. (1998). Interferometric estimation of three-dimensional ice-flow using ascending and descending passes. *IEEE Transactions on Geoscience and Remote Sensing*, 36(1):25–37.

Kratzsch, H. (1983). *Mining subsidence engineering*. Springer Science & Business Media.

Massonnet, D. and Feigl, K. L. (1998). Radar interferometry and its application to changes in the earth's surface. *Reviews of Geophysics*, 36(4):441–500.

Mattar, K. E., Vachon, P. W., Geudtner, D., Gray, A. L., Cumming, I. G., and Brugman, M. (1998). Validation of Alpine glacier velocity measurements using ERS tandem-mission SAR data. *IEEE Transactions on Geoscience and Remote Sensing*, 36(3):974–984.

Mohr, J. J. (1997). *Repeat Track SAR Interferometry. An investigation of its Utility for Studies of Glacier Dynamics*. PhD thesis, Technical University of Denmark, Copenhagen.

Mohr, J. J., Reeh, N., and Madsen, S. N. (1998). Three-dimensional glacial flow and surface elevation measured with radar interferometry. *Nature*, 291:273–276.

Müller, D. and Preusse, A. (2018). Use of the area of main influence to fix a relevant boundary for mining damages in germany. *International Journal of Mining Science and Technology*, 28(1):79–83.

Newton, I. (1687). *Philosophiae Naturalis Principia Mathematica*. Royal Society, London.

Notti, D., Herrera, G., Bianchini, S., Meisina, C., García-Davalillo, J. C., and Zucca, F. (2014). A methodology for improving landslide PSI data analysis. *International Journal of Remote Sensing*, 35(6):2186–2214.

Özer, I. E., van Leijen, F. J., Jonkman, S. N., and Hanssen, R. F. (2019). Applicability of satellite radar imaging to monitor the conditions of levees. *Journal of Flood Risk Management*, 12(S2):e12509.

Pöttgens, J. (1985). Uplift as a result of rising mine waters. In *The Development Science and Art of Mineral Surveying, Proceedings of the 6th International Congress. International Society for Mine Surveying, Harrogate UK*, volume 2.

Teunissen, P. J. G. (2003). *Adjustment theory*. VSSD Delft.

Titterton, D., Weston, J. L., and Weston, J. (2004). *Strapdown inertial navigation technology*, volume 17. IET.

Van Bergen, F., Pagnier, H., and Van Tongeren, P. (2007). Peat, coal and coalbed methane. *Geology of the Netherlands. Royal Netherlands Academy of Arts and Sciences*, pages 265–282.

van Leijen, F. J. (2014). *Persistent Scatterer Interferometry based on Geodetic Estimation Theory*. Number 86 in Publications on Geodesy. NCG. 195 pp.

Van Natijne, A., Bogaard, T., van Leijen, F., Hanssen, R., and Lindenbergh, R. (2022). World-wide InSAR sensitivity index for landslide deformation tracking. *International Journal of Applied Earth Observation and Geoinformation*, 111:102829.

Wright, T. J., Parsons, B. E., and Lu, Z. (2004). Towards mapping surface deformation in three dimensions using InSAR. *Geophysical Research Letters*, 31:5 pp.

Yu, B., Liu, G., Zhang, R., Jia, H., Li, T., Wang, X., Dai, K., and Ma, D. (2013). Monitoring subsidence rates along road network by persistent scatterer SAR interferometry with high-resolution TerraSAR-X imagery. *Journal of Modern Transportation*, 21:236–246.

A The projector $P^R_{\mathrm{LoS}^\perp}$

Eq. (2) contains $P^R_{\mathrm{LoS}^\perp}$, the projector that projects the displacement vector d_{TLN} onto the LoS along a plane orthogonal to the LoS. $P^R_{\mathrm{LoS}^\perp}$ is a function of Λ, Ω, and Φ with size 3×1, i.e., $P^R_{\mathrm{LoS}^\perp} = [P_T, P_L, P_N]$, with

$$
\begin{aligned}
P_T =& \big(\sin\theta \sin\alpha_d \cos\Lambda - \sin\theta \cos\alpha_d \sin\Lambda\big) \cos\Omega - \\
& \big(-(\sin\theta \sin\alpha_d \sin\Lambda + \sin\theta \cos\alpha_d \cos\Lambda) \sin\Phi + \cos\theta \cos\Phi\big) \sin\Omega \\
P_L =& \big(\sin\theta \sin\alpha_d \sin\Lambda + \sin\theta \cos\alpha_d \cos\Lambda\big) \cos\Phi + \cos\theta \sin\Phi \\
P_N =& \big(\sin\theta_m \sin\alpha_d \cos\Lambda - \sin\theta \cos\alpha_d \sin\Lambda\big) \sin\Omega + \\
& \big(-(\sin\theta_m \sin\alpha_d \sin\Lambda + \sin\theta \cos\alpha_d \cos\Lambda) \sin\Phi + \cos\theta \cos\Phi\big) \cos\Omega.
\end{aligned}
$$